01 Oct 2019

The Effect of Tantalum Incorporation on the Physical and Chemical Properties of Ternary Silicon–calcium–phosphorous Mesoporous Bioactive Glasses

Andrew Mendonca

Md Saidur Rahman

Adel Alhalawani

Omar Rodriguez

et. al. For a complete list of authors, see https://scholarsmine.mst.edu/che_bioeng_facwork/1079

Recommended Citation

Society For Biomaterials

The effect of tantalum incorporation on the physical and chemical properties of ternary silicon–calcium–phosphorous mesoporous bioactive glasses

Andrew Mendonca,[1,2] **Md. Saidur Rahman,**[2,3] **Adel Alhalawani,**[2,3] **Omar Rodriguez,**[2,3] **Reid C. Gallant,**[2] **Heyu Ni,**[4,5] **Owen M. Clarkin,**[6] **Mark R. Towler**[2,3]

[1]Department of Biomedical Engineering, Ryerson University, Toronto, M5B 2K3, Ontario, Canada
[2]Li Ka Shing Knowledge Institute, St. Michael's Hospital, Toronto, M5B 1W8, Ontario, Canada
[3]Department of Mechanical and Industrial Engineering, Ryerson University, Toronto, M5B 2K3, Ontario, Canada
[4]Canadian Blood Services Centre for Innovation, Toronto, M5G 2M1, Ontario, Canada
[5]Department of Laboratory Medicine and Pathobiology, University of Toronto, Toronto, M5S 1A1, Ontario, Canada
[6]School of Mechanical & Manufacturing Engineering, Dublin City University, Dublin, Ireland

Abstract: Synthesis and characterization of the first mesoporous bioactive glasses (MBGs) containing tantalum are reported here, along with their potential application as hemostats. Silica MBGs were synthesized using with the molar composition of (80-x)% Si, 15% Ca, 5% P, and x% Ta. It was found that incorporation of >1 mol % Ta into the MBGs changes their physical and chemical properties. Increasing Ta content from 0 to 10 mol % causes a decrease in the surface area and pore volume of ~20 and ~35%, respectively. This is due to the increase in nonbridging oxygens and mismatch of thermal expansion coefficient which created discontinuities in the ordered channel structure.

However, the effect is not significant on the amount of ions (Si, Ca, P, and Ta) released, from the sample into deionized water, for short durations (<60 min). In a mouse tail-cut model, a significant decrease in bleeding time (≥50% of average bleeding time) was found for Ta-MBGs compared to having no treatment, Arista, and MBG without Ta. Further studies are proposed to determine the mechanism of Ta involvement with the hemostatic process. © 2019 Wiley Periodicals, Inc. J Biomed Mater Res B Part B: Appl Biomater 107B:2229–2237, 2019.

Key Words: mesoporous bioactive glass, tantalum, hemostasis

INTRODUCTION

Bioactive glasses (BGs) were first synthesized by Hench et al. and are capable of chemically bonding with host tissue.[1] Their bioactivity stems from ion release which can promote the development of a hydroxyapatite (HA) layer at the interface of the implant upon maturation in an aqueous medium.[2] The HA develops from an exchange of ions between the glass and the medium resulting in the buildup of crystalline calcium phosphate compounds on the surface.[1]

Mesoporous bioactive glasses (MBGs) are a subset of BGs that possess a mesoporous channel structure.[3] This gives them high specific surface area, significantly greater than that of melt-quenched BGs of similar composition.[4] Bioactivity is proportionally influenced by specific surface area; therefore, MBGs can be designed with high bioactivity.[2] Silica-based MBGs have an amorphous structure which can accommodate various ions as network modifiers[5] which disrupt the continuity of the glass network and form nonbridging silicon–oxygen bonds (Si-NBO). The number of Si-NBOs affects the bioactivity of the glasses, with increased numbers of Si-NBO bonds leading to greater reactivity.[5] Network modifiers can further influence glass properties depending on the ion used. For example, calcium (Ca) ions can accelerate blood coagulation.[6] MBGs with silver (Ag) ions can be antibacterial[7–9] against Gram-negative and Gram-positive bacteria even at 0.02 wt % Ag. MBGs with europium (1–5 mol %) have shown significant bone formation stimulation in an *in vivo* rat model.[10] Gallium (Ga)-doped MBGs have been shown to be potential hemostatic agents and also exhibit antibacterial properties[11]; low amounts of Ga (5–10 mg of 1–3 mol % Ga-MBGs) induces the intrinsic pathway of the blood coagulation cascade and can inhibit bacterial growth of *Escherichia coli* and *Staphylococcus aureus.*

Hemostats are agents that stop bleeding from a damaged blood vessel.[12] Commercially available hemostats work by one, or a combination, of two mechanisms: (1) sealing the damaged blood vessels, and (2) concentrating clotting factors and

Correspondence to: M. Tower; e-mail: mtowler@ryerson.ca

initiating the intrinsic blood coagulation pathway.[13] Such hemostats can be classified as either organic or inorganic depending upon their composition. Organic hemostats are usually based on gelatin, cellulose, and chitosan.[12] However, these products have some inherent drawbacks: animal gelatin containing hemostats, for example, GELFOAM (Pfizer Inc., New York, NY), can cause serious allergic reactions and lead to anaphylaxis,[14] HemCon (Tricol Biomedical Inc., Portland, OR), a chitosan-based hemostat synthesized from shrimp shells is unsuitable for deep wounds or irregular wound surfaces due to the rigidity of the dressing[15]; and Arista (C. R. Bard Inc., Delran, NJ), a starch-based hemostat, swells on application, which has been reported to lead to tissue compression and necrosis, making it unsuitable for use in enclosed spaces such as near small blood vessels.[12,16] Inorganic hemostats are typically clay or zeolite based.[17] Zeolites possess a microporous structure, usually with a pore diameter less than 2 nm, and can absorb high amounts of water which reduces clotting time (>25 min) by concentrating clotting factors.[18] However, zeolite-based hemostats can cause an exothermic reaction at the wound site with tissue temperatures capable of rising to 90°C.[13] Combat Gauze (Z-Medica LLC, Wallingford, CT) is a cotton gauze implanted with kaolin that initiates the intrinsic pathway of the blood coagulation cascade.[19] The initiation requires blood to reach kaolin through the gauze and so it is slower in achieving hemostasis compared to other inorganic counterparts.[13] These hemostats have all been shown to reduce bleed time, but have major side effects or drawbacks that limit their use to certain situations. There is a drive toward developing an all-purpose hemostat that can be applied in any situation with no side effects.

This manuscript presents tantalum (Ta) containing MBGs (Ta-MBGs) for the first time, building upon earlier work by Pourshahrestani et al.[11] who investigated the role of gallium (Ga) in MBGs. Ta was identified as a potential hemostat because it has previously been used in hemostatic clips[20] while tantalum oxide (Ta_2O_5) powder, containing low amounts of iron, has been used as a wound dressing to accelerate blood clotting and prevent bacterial infection.[21] The objectives of this study are to synthesize (80-x)Si-15Ca-5P-xTa mol % MBGs with increasing amounts of Ta, characterize their structure, and evaluate the effect of the morphology and Ta content on ion release and hemostasis (clotting time) in a mouse tail-cut model.

MATERIALS AND METHODS
Materials
Reagent grade triblock copolymer P123, calcium nitrate tetrahydrate, triethyl phosphate (TEP), tetraethyl orthosilicate (TEOS), tantalum(V) ethoxide, and ethanol (EtOH) were used. Reagent grade hydrochloric acid (HCl) was diluted to 0.5 M HCl using distilled water. All reagents were obtained from Sigma Aldrich, Oakville, Canada. A surface directing agent was used to make the mesoporous structure. In this case, P123 was the chosen agent because it yields well-ordered, 2D hexagonal channels.[22] Arista, a commercial starch-based hemostat, was purchased from C. R. Bard Inc. to use as a control for the hemostasis model.

Synthesis
MBGs were synthesized with incremental Ta content, at the expense of silicon (Si), according to Table I. Calcium (Ca) and phosphorous (P), incorporated to increase bioactivity through apatite formation, are kept constant through all the samples.

Synthesis of MBGs was performed using the method outlined by Yan et al.[3] Typically, 4 g of P123 and 1.4 g of calcium nitrate tetrahydrate were dissolved in 76 mL of ethanol. In a separate graduated cylinder, 1 mL of 0.5 M HCl and an appropriate amount of TEOS were allowed to react for the acid-catalyzed hydrolysis of TEOS. Since TEOS amount determined the Si content in the final MBG, the amount varied corresponding to the sample being made. Then, 0.68 mL TEP and appropriate amount of tantalum(V) ethoxide were added to the ethanol solution. Finally, the TEOS-acid solution was slowly poured into the ethanol solution.

The solution was covered and stirred overnight. It was then transferred to a Petri dish for 5 days to allow for the evaporation-induced self-assembly (EISA) process. The EISA-derived gel was then calcined at 650°C, holding for 6 h. The ramp rate used for the furnace was 1 °C/min. The resultant MBGs were ground and sieved with a 45 μm mesh.

X-ray diffraction
Wide-angle X-ray diffraction (WAXRD) patterns were collected using a Philips PW3710 X-ray diffractometer (Phillips, Holland) with a Cu source from 5° to 160° (2θ), at a step size of 0.1°. A generator voltage of 45 kV and a tube current of 20 mA were employed.

Small-angle X-ray diffraction (SAXRD) was carried out to confirm whether ordered mesoporous channels were present. SAXRD patterns were collected using an Anton Parr SAXS diffractometer (Anton Paar, Austria) with a Cu source from 0.2° to 10° (2θ), at a step size of 0.04°. A generator voltage of 40 kV and a tube current of 50 mA were employed.

Energy dispersive X-ray spectroscopic analysis and X-ray photoelectron spectroscopy
A JEOL 6380LV scanning electron microscope (SEM; JEOL, Peabody, MA) equipped with Oxford energy dispersive X-ray spectroscopy (EDS) was used to qualitatively examine the chemical composition of each sample. A 1 cm Cu sample holder with double-sided carbon tape was pressed onto powder samples and placed into the SEM for analysis.

X-ray photoelectron spectroscopy (XPS) was conducted on a K-Alpha XPS system (Thermo Fisher Scientific, Waltham, MA). Monochromated Al K-Alpha X-rays were used for

TABLE I. Compositions of Synthesized Mesoporous Bioglasses (mol %)

Sample Code	Ta	Si	Ca	P
MTa-0	0	80	15	5
MTa-0.5	0.5	79.5	15	5
MTa-1	1	79	15	5
MTa-5	5	75	15	5
MTa-10	10	70	15	5

analysis, with a spot size of 400 μm. Charge compensation was achieved utilizing a low energy flood of electrons and ions under $\sim 5 \times 10^{-8}$ mbar vacuum. Residual pressure was from argon associated with operation of a charge compensation source. The survey spectrum was acquired in a high-pass energy (200 eV), low point-density (1 point/eV) scanned mode. Regional spectra, used to determine relative atomic composition, as well as for determination of chemical information, was acquired in a low-pass energy (50 eV), high point-density (0.1 eV spacing) scanned mode. Analysis was calibrated using the C1s peak and binding energy of 284.8 eV.

Fourier transform infrared spectroscopy

Fourier transform infrared spectroscopy (FTIR) was carried out on the powder samples using an ATR-iS50 FTIR (Thermo Scientific). Spectra were collected from 400 to 1500 cm^{-1} with 0.25 cm^{-1} resolution.

Transmission electron microscopy

Transmission electron microscopy (TEM) was carried out on a Hitachi HT-7700 (Hitachi, Japan), to analyze the nanochannels within the glass. Samples were embedded in modified Spurr's resin (Electron Microscopy Sciences, Hatfield, PA), ultramicrotomed to 100 nm thick slices, and then placed on copper grids for imaging. Imaging was carried out at 80 kV and an emission current of ~10 μA.

Brunauer–Emmett–Teller and Barrett–Joyner–Halenda analysis

Surface area measurements were carried out by nitrogen gas adsorption in a Micromeritics Gemini VII 2390 gas adsorption analyzer (Micromeritics, Norcross, GA). The surface area was then calculated using Brunauer, Emmett, and Teller (BET), and pore size distribution and pore volume were estimated using the Barrett–Joyner–Halenda (BJH) schema.

Ion release analysis

Ion release was conducted in deionized (DI) water and analyzed using inductively coupled plasma-optical emission spectroscopy (ICP-OES). Total of 50 mg of sample was placed in a microcentrifuge tube containing 1 mL DI water. After the appropriate time intervals (15, 30, and 60 min), samples were centrifuged at 10,000 rpm for 2 min.[23] The supernatant was collected and diluted to conduct analyses. Three samples of each glass were taken, at each time interval.

Chemical compositions of the collected samples were analyzed using ICP-OES, performed on an Optima 7300 DV ICP-OES (Perkin Elmer, Waltham, MA). Calibration standards for silicon, calcium, and phosphorus were prepared from a 1000 ppm stock solution. For silicon sample 1, 5, 10, and 25 ppm were used as calibration standards. For calcium and tantalum 0.5, 1, 5, and 10 ppm, and for phosphorous 0.1, 0.5, and 1, 5 ppm calibration standards were used. In all cases, DI water was used as the blank. The machine ran each calibration solution and sample three times.
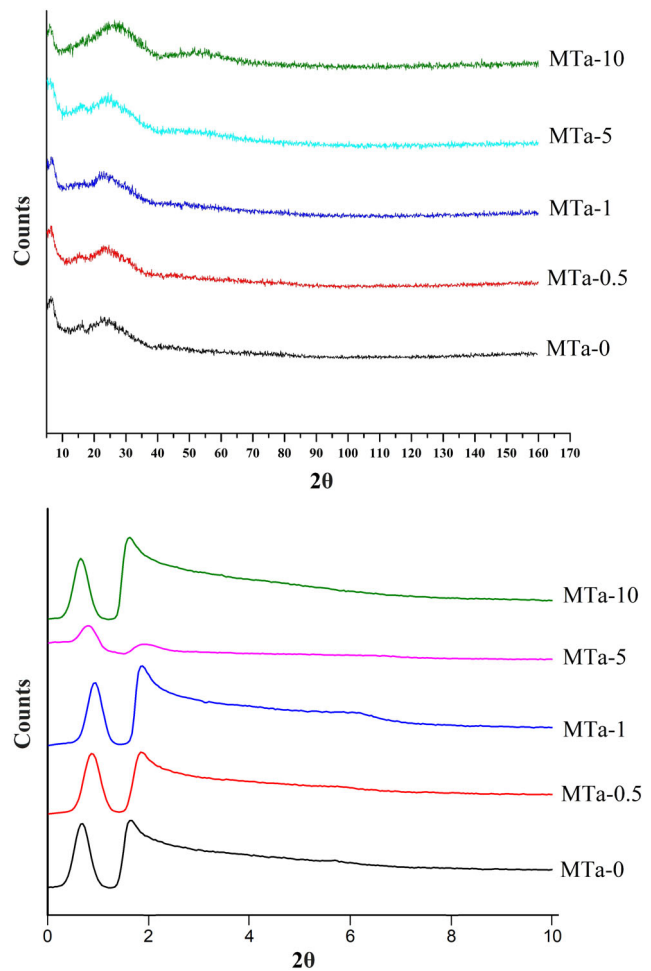

FIGURE 1. XRD results for MBG samples; no significant peaks are seen.

TABLE II. Composition of MBG Samples from EDS Data (wt %)

Sample	O	Si	Ca	P	Ta
MTa-0	58.6	31.4	7.2	2.8	0
MTa-0.5	55.5	31.2	8.0	2.5	2.8
MTa-1	58.2	27.9	6.7	2.1	5.1
MTa-5	47.6	23.6	6.0	1.8	21.0
MTa-10	37.7	20.2	5.3	1.2	35.6

Hemostasis model

To evaluate the hemostatic performance of the MBGs, a tail-cut model was used.[24] The trials were approved by the St. Michael's Hospital research ethics board (St. Michael's Hospital, Toronto, Canada). Wild-type c57bl/6 mice, 6–8 weeks

TABLE III. Theoretical wt % of MBG Compositions

Sample	O	Si	Ca	P	Ta
MTa-0	50.3	35.3	9.5	4.9	0.0
MTa-0.5	49.2	34.1	9.5	4.7	2.8
MTa-1	48.2	32.9	8.9	4.6	5.4
MTa-5	41.6	25.5	7.3	3.7	21.9
MTa-10	36.2	19.3	5.9	3.0	35.6

TABLE IV. Normalized XPS Data of MBG Compositions (wt %)

Sample	O	Si	Ca	P	Ta
MTa-0	45.9	45.7	5.2	3.1	0.0
MTa-0.5	45.4	43.9	6.4	2.6	1.8
MTa-1	44.0	41.7	6.3	2.6	5.4
MTa-5	35.8	31.2	4.6	2.4	26.1
MTa-10	27.1	21.9	3.9	0.9	46.2

old, were housed at the hospital facilities and given unrestricted access to food and water. Prior to tail transection, mice were anesthetized *via* intraperitoneal injection with 10 μL/g bodyweight of tribromoethanol (Avertin). Tail transection was performed 5 mm from the tip with a scalpel. For all treatment samples, the injury was coated evenly with samples of glass or Arista and mice were then placed on top of a platform with the tail hanging over the edge. The time was recorded, and the
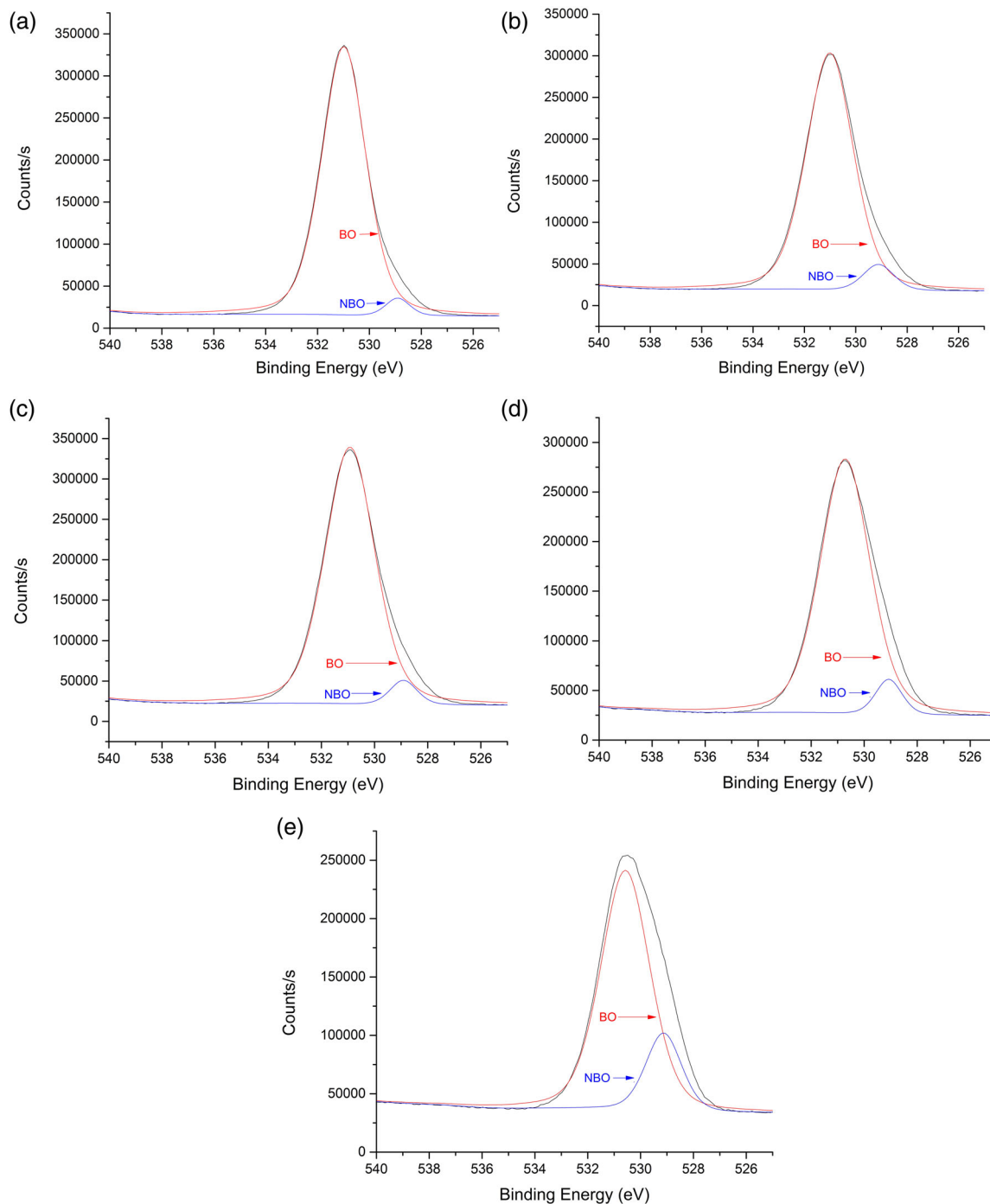
FIGURE 2. High resolution O1s spectrum for (a) MTa-0, (b) MTa-0.5, (c) MTa-1, (d) MTa-5, and (e) MTa-10. The graphs show the BO peak, NBO peak, and the combined peak. As Ta content is increased, the NBO content increases.

TABLE V. BO and NBO Binding Energy, Atomic Percentage, and Change in Energy for MBG Samples

|	BO		NBO		
Sample	Binding Energy (eV)	atm %	Binding Energy (eV)	atm %	Δ binding Energy (eV)
MTa-0	530.98	96.46	528.88	3.54	2.1
MTa-0.5	530.98	93.09	529.08	6.91	1.9
MTa-1	530.88	94.95	528.88	5.05	2
MTa-5	530.68	92.94	529.08	7.06	1.6
MTa-10	530.58	84.85	529.08	18.15	1.5

tail dabbed onto blotting paper every 15 s (from transection) until bleeding ceased. The time required for bleeding to stop was reported as the bleeding time. Mice were randomly treated with MBG samples ($n = 5–10$ for each MBG), Arista ($n = 5$), or no treatment ($n = 9$). Since the mice age spanned a couple weeks between the start and end of testing, extra mice were tested intermittently without treatment to see whether the age caused a variation in the data. All the data fell within the initial range measured for $n = 5$. Tests of the MTa-0 material were repeated ($n = 5$) because they initially showed no significant difference from the absence of treatment, and a retrial was performed to ensure no experimental error had taken place. Results were similar to the first set of tests.

Statistical analysis

Statistical analysis was performed using SPSS software (IBM SPSS Statistics, version 24, Armonk, NY). Independent samples t test was used to analyze the data and to find out statistical significance with $p < 0.05$.

RESULTS

Figure 1 shows the XRD patterns from the MBG samples. The top image shows the WAXRD results and that no significant peaks are found in the traces. The bottom image shows
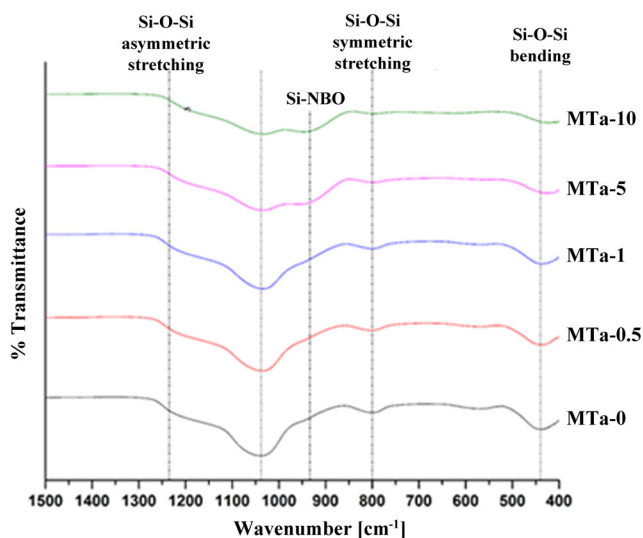
FIGURE 3. FTIR spectra of MBGs with corresponding silicon bonds. Increasing Ta decreases Si bonds except the Si-NBO.

the SAXRD results for the MBG samples. All samples exhibited two diffraction peaks in the range from 0.2° to 2° which are characteristic of the P6mm space group[25] in hexagonal crystal systems. The slight shift in the peaks is due to the changes in pore diameters and pore volumes between the samples.

EDS results in Table II show the chemical composition of MBG samples. Results show increasing Ta content indicating that incorporation of Ta in the samples is assured. Specific data values (Table II) are different from theoretical values (Table III) due to the presence of extra oxygen from moisture in the atmosphere; the vacuum used while running EDS is insufficient to ensure the removal of all moisture from the samples. This causes an overall decrease in the wt % of the other elements present.

Wide-scan XPS was conducted and atomic percentages (normalized without carbon) are shown in Table IV for different MBG samples. Values presented here vary from the ones shown in Table III. The Ta 4d peak was chosen for analysis since its peak has the least interference with other elements present and its intensity is high enough to ensure reliable data.

High resolution O1s spectra for the MBG samples are exhibited in Figure 2 with details of peak intensities in Table V. The O1s peaks can be seen as a superposition of two individual peaks: the bridging oxygens (BO) and the nonbridging oxygens (NBO) found in the sample. It is observed that the overall O1s peak shifts to lower binding energy because of increasing number of NBOs. Since electron charge density is higher in NBO, it reduces its effective binding energy, relative to BO. For most samples, the amount of NBO is relatively the same until the 10% Ta incorporation.

FTIR transmission spectra are shown in Figure 3 along with corresponding peaks. The peak at 440 cm^{-1} represents Si-O-Si bending vibration,[26] whereas the peak at 800 cm^{-1} indicates symmetric stretching of Si-O bond.[27] Characteristic peaks located at 1038 and 1235 cm^{-1} are attributed to asymmetric stretching of Si-O bond.[28] Finally, the peak observed at 934 cm^{-1} is identified as Si-NBO.[29] From the FTIR spectra, the intensity of the stretching and bending bonds of silicon decreased with increasing tantalum content. However, it should be noted that the intensity of the Si-NBO bond increases when 5% and higher Ta is mixed in.

TEM micrographs of the MBGs are represented in Figure 4. In the images, well-ordered 2D hexagonal mesoporous channels are observed in MBGs containing up to 0.5% Ta [Fig. 4(a,b)]. However, MBGs with higher Ta content have disruptions in ordered channels [Fig. 4(c)]. It is difficult to quantify the extent of disruption but surface area gives an indication of the magnitude. Table VI shows the surface area and pore volumes of the corresponding samples. As expected, the surface area decreases as the tantalum content increases. Pore diameter and volume also decrease, with the exception of pore volume for MTa-5.

Ion release profiles for MBGs are plotted in Figure 5. Concentration of Ca, P, Si, and Ta ions were measured 15, 30, and 60 min after soaking in DI water. These time
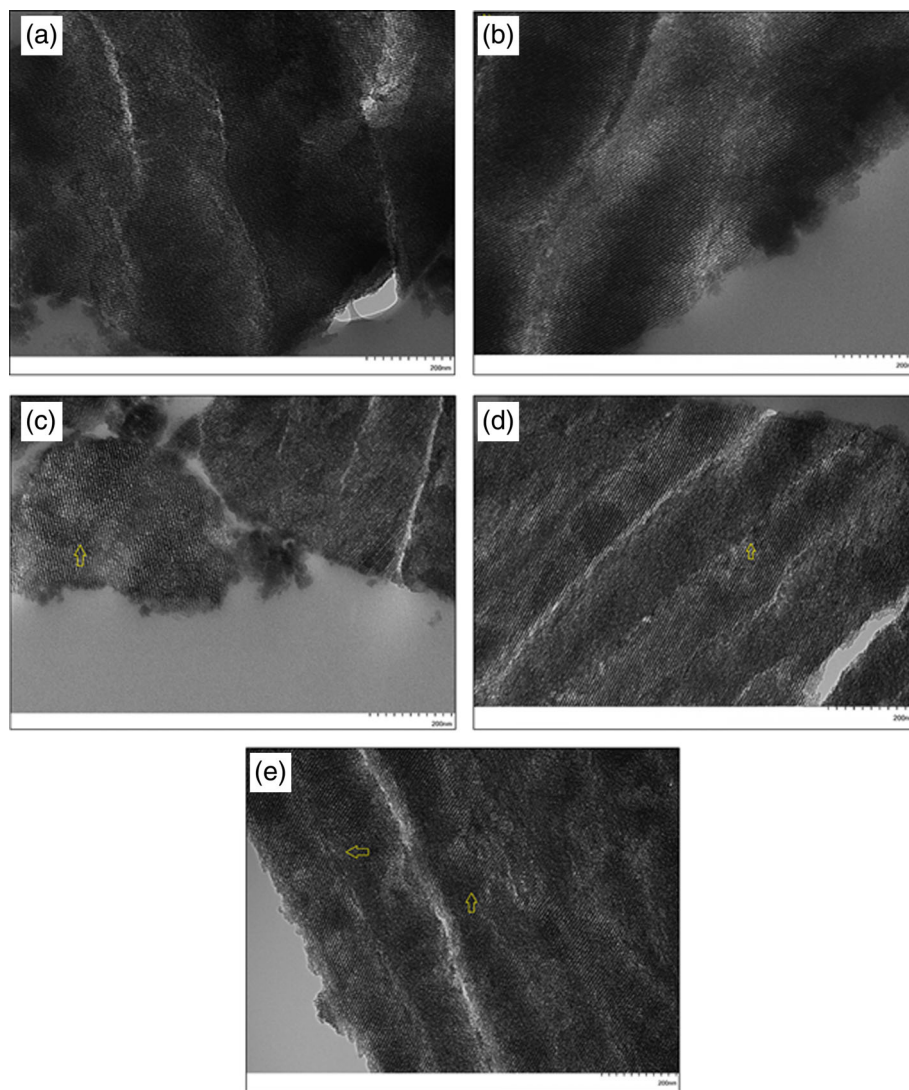
FIGURE 4. TEM images of (a) MTa-0, (b) MTa-0.5, (c) MTa-1, (d) MTa-5, and (e) MTa-10 glasses. Arrow sign indicates discontinuity in the channel. The 2D hexagonal framework incurs more discontinuities as the Ta content increases, as can be seen in MTa-1, MTa-5, and MTa-10.

intervals were chosen based on the application of MBGs in hemostasis, as platelet plug formation in primary hemostasis occurs within an hour.[30] There are two main trends that can be seen in the data. First, the Si ion concentration goes down as Ta ion content goes up. Second, ion concentrations did not change significantly from the 15 min mark to the 60 min mark for tantalum and calcium.

TABLE VI. BET Surface Area and, BJH Pore Volume, and Pore Diameter of all Samples

Sample	Surface Area (m^2/g)	Pore Volume (cm^3/g)	Pore Diameter (nm)
MTa-0	373.87	0.2677	4.3
MTa-0.5	373.98	0.2151	4.2
MTa-1	353.14	0.2063	4.1
MTa-5	328.44	0.2293	4.0
MTa-10	297.55	0.1702	3.9

The tail bleeding time was used as a hemostasis model; results are shown in Figure 6. The plot shows a noticeable decrease in mean bleeding time of mice treated with Ta containing samples compared to the controls (no treatment, Arista, and MBG without Ta). The significance of these results is shown in Table VII. There is no significant difference between no treatment, Arista, and the MTa-0 glass. However, there is a significant difference between the Ta containing glasses and no treatment, Arista, and MTa-0. The only exception is between MTa-1 and Arista which has a p value of 0.06.

DISCUSSIONS

A series of MBGs were successfully synthesized and characterized in terms of their composition, structure and porosity. Preliminary work on hemostatic effects was also conducted using a tail-cut model. We hypothesized that Ta has a positive effect on hemostasis and, that increasing Ta content
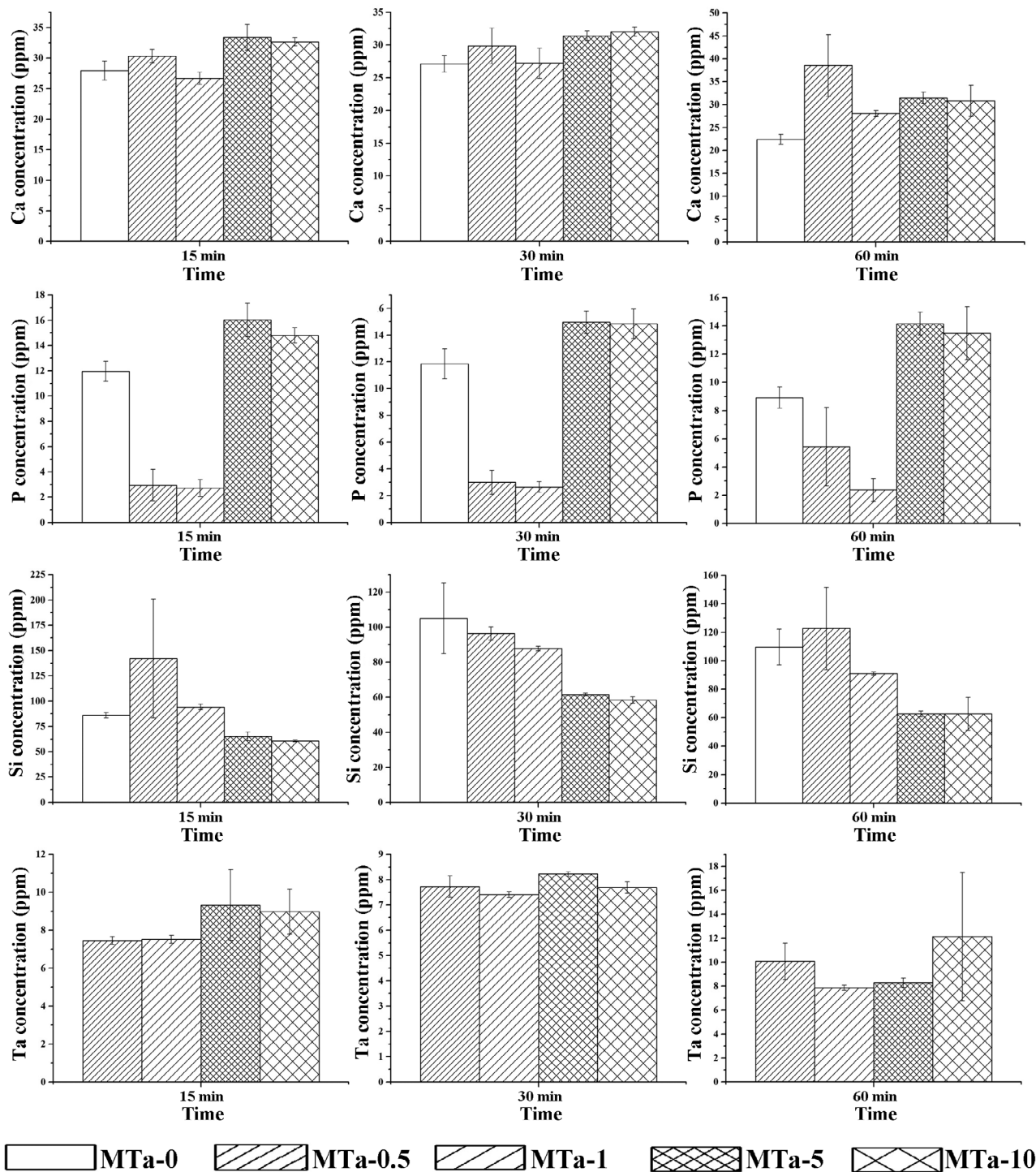
FIGURE 5. Ion release profiles from MBGs for silicon, calcium, phosphorous, and tantalum ions. No significant trends can be seen besides decreasing Si with increasing Ta.

would result in higher amounts of ions released in aqueous media and improved hemostatic effect over a Ta-free MBG control.

WAXRD shows that all glasses are amorphous and do not crystallize with the incorporation of Ta. EDS and XPS data confirm the incorporation of Ta into the glass structure. However, EDS showed greater incorporation of calcium than

was shown in the XPS data. The reason for this is that XPS measures surface composition and penetrates only a few nanometers into the sample. It has been shown that Ca concentrations are higher in the bulk compared to the surface[31] and as a result XPS would not reflect Ca^{2+} ion concentrations accurately. Due to Ta having a much higher molecular weight compared to Ca (181 g/mol compared to 40 g/mol), a small
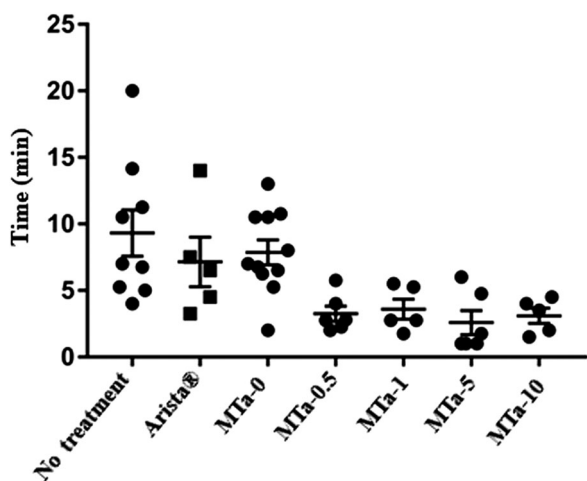
FIGURE 6. Tantalum containing BGs decreased the tail bleeding time in c57bl/6 mice. Results from hemostasis model are represented with individual symbols (•) representing one mouse; error bars represent standard error of the mean (n = 5–10).

molar increase of Ta on the surface leads to a much higher wt % of Ta in the sample's result. Therefore, the Ta content in the XPS results (Table IV) is 5–10% higher than the theoretical values in Table III.

FTIR peaks, corresponding to the silicon–oxygen bonds present in the glass matrices, have expected trends. Across the series, increasing Ta content reduces the intensity of Si-O bending, symmetric and asymmetric stretching peaks. Conversely, increasing Ta concentration increases the intensity of the Si-NBO bonding peak. This result is also confirmed by the XPS O1s spectra. The increasing Si-NBO bonds are from Si-O-Si getting replaced by Si-O-Ta.[32]

Characterization of the mesostructure and porosity of the MBGs was performed using SAXRD, TEM and nitrogen adsorption. SAXRD shows peaks found from the repeating mesoporous nanostructure of the p6mm space group of hexagonal lattice systems. TEM imaging gave visual confirmation of the inner structure whereas the BET and BJH schema quantified specific surface area and pore volume. There is a slight right shift of the SAXRD peaks, caused from a decrease in pore diameter, as seen in MTa-0 to MTa-1 in Figure 1 (bottom); this pore diameter decrease is confirmed by the BJH data. However, MTa-5 and MTa-10 have a slight left shift of their peaks. This may be due to the discontinuities in the channel structure, observed in TEM, and the broken channels appearing as larger channels when diffracting the X-rays. Comparing TEM images of each set of glasses, the

MBGs keep an ordered hexagonal structure up to ~1% Ta incorporation. At this point, discontinuities appear in the channel structure as visible breaks. This increases as the Ta content is increased, with 10% Ta having the most discontinuities in the structure [Fig. 4(e)] relative to the others. The authors postulate that these discontinuities arise due to the mismatch in the coefficient of thermal expansion (CTE) of the Ta relative to the other MBG materials. Using estimate models of CTE from Bellucci et al., with Hall coefficients,[33] it is calculated that the CTE for MTa-0 is 3.08×10^{-6} K^{-1}. This is less than half of that of Ta which is 6.7×10^{-6} K^{-1}.[34] The Hall coefficients were chosen based on the conclusions of Bellucci et al., and the fact that the coefficients were determined at high temperatures (comparable to the calcination temperatures used in this work). Due to the CTE of Ta being so large, it would have a greater change in volume relative to the surrounding structure. This sudden change, when going from the 650°C of calcination to room temperature, could cause nanoscale defects in the structure. With bulk BGs, these nanoscale defects are sufficient to significantly increase the ion solubility of the glasses in aqueous medium.[35] Therefore, in MBGs, where the channels are just an order of magnitude greater than the defect size, the effect of nanoscale defects is more prominent and causes breaks in the channel structure.

Ion release analysis (Fig. 5) did not indicate any significant trends with Ta incorporation. There is a decrease in the amount of Si released (with increasing Ta content) but that is expected due to the decreasing Si content in the as-produced glasses. A likely explanation for such small changes in the amount of ions released is because the time interval chosen (based on what is relevant to the hemostatic application[30]) was too short for a high release of ions; no steady-state point was identified in the ion release analysis.

Bleeding times from the hemostasis model demonstrate, that compared to controls (no treatment, MBG with no Ta, or the commercial hemostat Arista), Ta-containing MBGs significantly decrease the tail bleeding time. It was postulated that the physical morphology of MBGs will have a large effect on the initial hemostatic response by sequestering water and increasing the concentration of coagulation factors. This is the same mechanism with which Arista has been shown to promote hemostasis.[36] However, Arista swells with the water incorporation whereas the MBGs retain their size. Both Arista and the MTa-0 glass showed no significant decrease in hemostasis time when compared to the absence of treatment. This suggests that the hypothesis considering Ta accelerating the coagulation process is correct; either

TABLE VII. Significance (p values) Between Mean Tail Bleeding Times from the Hemostasis Model

	No Treatment	Arista	MTa-0	MTa-0.5	MTa-1	MTa-5	MTa-10
No treatment	x	0.22	0.22	0.01	0.02	0.01	0.01
Arista		x	0.35	0.03	0.06	0.02	0.04
MTa-0			x	<0.01	0.01	<0.01	<0.01
MTa-0.5				x	0.36	0.27	0.43
MTa-1					x	0.21	0.31
MTa-5						x	0.33

EFFECT OF TANTALUM INCORPORATION ON THE PHYSICAL AND CHEMICAL PROPERTIES

directly (through chemical reactions with the coagulation factors), indirectly (affecting the reactivity of the glasses), or a combination of both.

CONCLUSIONS

Incorporation of Ta into Si-Ca-P MBGs creates discontinuities in the channel structure when incorporated at ~1 mol % or more. These are likely due to defects in the mesoporous glass structure from the substitution of Ta for Si, and mismatching corresponding CTEs. Increasing the Ta content causes a decrease in the surface area and pore volume of the glasses; however, the effect on ion release is minimal when MBGs are matured in DI water for less than 60 min. Tantalum containing MBGs show promise as potential hemostatic agents, outperforming the commercial hemostat Arista and MBG without Ta in a mouse tail-cut model.

REFERENCES

1. Hench LL, Splinter RJ, Allen WC, Greenlee TK. Bonding mechanisms at the interface of ceramic prosthetic materials. J Biomed Mater Res 1971;5:117–141.
2. Vichery C, Nedelec J-M. Bioactive glass nanoparticles: From synthesis to materials design for biomedical applications. Materials 2016;9:288–305.
3. Yan X, Yu C, Zhou X, Tang J, Zhao D. Highly ordered mesoporous bioactive glasses with superior in vitro bone-forming bioactivities. Angew Chem Int Ed 2004;43:5980–5984.
4. Wu C, Chang J. Mesoporous bioactive glasses: Structure characteristics, drug/growth factor delivery and bone regeneration application. Interface Focus 2012;2:292–306.
5. González P, Serra J, Liste S, Chiussi S, León B, Pérez-Amor M. Raman spectroscopic study of bioactive silica based glasses. J Non Cryst Solids 2003;320:92–99.
6. Lovelock JE, Porterfield BM. Blood clotting: The function of electrolytes and of calcium. Biochem J 1952;50:415–420.
7. Hu G, Xiao L, Tong P, Bi D, Wang H, Ma H, Zhu G, Liu H. Antibacterial hemostatic dressings with nanoporous bioglass containing silver. Int J Nanomedicine 2012;7:2613–2620.
8. Phetnin R, Rattanachan ST. Preparation and antibacterial property on silver incorporated mesoporous bioactive glass microspheres. J Sol-Gel Sci Technol 2015;75:279–290.
9. Gargiulo N, Cusano AM, Causa F, Caputo D, Netti PA. Silver-containing mesoporous bioactive glass with improved antibacterial properties. J Mater Sci Mater Med 2013;24:2129–2135.
10. Baino F, Fiorilli S, Vitale-Brovarone C. Bioactive glass-based materials with hierarchical porosity for medical applications: Review of recent advances. Acta Biomater 2016;42:18–32.
11. Pourshahrestani S, Zeimaran E, Kadri NA, Gargiulo N, Samuel S, Naveen SV, Kamarul T, Towler MR. Gallium-containing mesoporous bioactive glass with potent hemostatic activity and antibacterial efficacy. J Mater Chem B 2015;4:71–86.
12. Spotnitz WD, Burks S. Hemostats, sealants, and adhesives: Components of the surgical toolbox. Transfusion 2008;48:1502–1516.
13. Kheirabadi B. Evaluation of topical hemostatic agents for combat wound treatment. US Army Med Dep J 2011;2:25–37.
14. Spencer HT, Hsu JT, McDonald DR, Karlin Ll. Intraoperative anaphylaxis to gelatin in topical hemostatic agents during anterior spinal fusion: A case report. Spine J Off J North Am Spine Soc 2012;12:e1–e6.
15. Schreiber MA, Neveleff DJ. Achieving hemostasis with topical hemostats: Making clinically and economically appropriate decisions in the surgical and trauma settings. AORN J 2011;94:S1–S20.
16. Offodile AC, Chen B, Aherrera AS, Guo L. Microporous polysaccharide hemospheres potentiate ischemia-induced skin flap necrosis in a murine model. Plast Reconstr Surg 2017;139:59e–66e.
17. Pourshahrestani S, Zeimaran E, Djordjevic I, Kadri NA, Towler MR. Inorganic hemostats: The state-of-the-art and recent advances. Mater Sci Eng C 2016;58:1255–1268.
18. Arnaud F, Tomori T, Carr W, McKeague A, Teranishi K, Prusaczyk K, McCarron R. Exothermic reaction in zeolite hemostatic dressings: QuikClot ACS and ACS+®. Ann Biomed Eng 2008;36:1708–1713.
19. Johnson D, Gegel B, Burgert J, Gasko J, Cromwell C, Jaskowska M, Steward R, Taylor A. The effects of QuikClot combat gauze, fluid resuscitation, and movement on hemorrhage control in a porcine model. ISRN Emerg Med 2012;2012:1–6.
20. Samuels PB, Roedling H, Katz R, Cincotti JJ. A new hemostatic clip: 2-year review of 1007 cases. Ann Surg 1966;163:427–431.
21. Olson CT, Hoffmann RW. Tantalum oxide composition [Internet]. 1949 [cited 2017 Dec 8]. Available from: http://www.google.com/patents/US2491416
22. Wu C, Chang J. Multifunctional mesoporous bioactive glasses for effective delivery of therapeutic ions and drug/growth factors. J Control Release 2014;193:282–295.
23. Majekodunmi SOA. Review on centrifugation in the pharmaceutical industry. Am J Biomed Eng 2015;5:67–78.
24. Greene TK, Schiviz A, Hoellriegl W, Poncz M, Muchitsch E-M. Towards a standardization of the murine tail bleeding model. J Thromb Haemost 2010;8:2820–2822.
25. Zhao D, Wan Y, Zhou W. Ordered Mesoporous Materials. Weinheim, Germany: Wiley-VCH; 2013. p. 522.
26. Barrioni BR, Oliveira AC, Leite M de F, Pereira M de M. Sol–gel-derived manganese-releasing bioactive glass as a therapeutic approach for bone tissue engineering. J Mater Sci 2017;52:8904–8927.
27. Philippart A, Boccardi E, Pontiroli L, Beltrán AM, Inayat A, Vitale-Brovarone C, Schwieger W, Spiecker E, Boccaccini AR. Development of novel mesoporous silica-based bioactive glass scaffolds with drug delivery capabilities. Adv Sci Technol 2014;96:54–60.
28. Serra J, González P, Liste S, Serra C, Chiussi S, León B, Pérez-Amor M, Ylänen HO, Hupa M. FTIR and XPS studies of bioactive silica based glasses. J Non Cryst Solids 2003;332:20–27.
29. Shah AT, Ain Q, Chaudhry AA, Khan AF, Iqbal B, Ahmad S, Siddiqi SA, ur Rehman I. A study of the effect of precursors on physical and biological properties of mesoporous bioactive glass. J Mater Sci 2015;50:1794–1804.
30. Boon GD. An overview of hemostasis. Toxicol Pathol 1993;21:170–179.
31. Pérez-Pariente J, Balas F, Vallet-Regí M. Surface and chemical study of $SiO_2 \cdot P_2O_5 \cdot CaO \cdot (MgO)$ bioactive glasses. Chem Mater 2000;12:750–755.
32. Alhalawani AMF, Towler MR. The effect of $ZnO \leftrightarrow Ta_2O_5$ substitution on the structural and thermal properties of SiO_2-ZnO-SrO-CaO-P_2O_5 glasses. Mater Charact 2016;114:218–224.
33. Bellucci D, Cannillo V, Sola A. Coefficient of thermal expansion of bioactive glasses: Available literature data and analytical equation estimates. Ceram Int 2011;37:2963–2972.
34. Hidnert P. Thermal expansion of tantalum. Bur Stand J Res 1929;2:887.
35. Alhalawani AM, Mehrvar C, Stone W, Waldman SD, Towler MR. A novel tantalum-containing bioglass. Part II. Development of a bioadhesive for sternal fixation and repair. Mater Sci Eng C 2017;71:401–411.
36. Murat F-JL, Ereth MH, Dong Y, Piedra MP, Gettman MT. Evaluation of microporous polysaccharide hemospheres as a novel hemostatic agent in open partial nephrectomy: Favorable experimental results in the porcine model. J Urol 2004;172:1119–1122.